



Article

Enhanced Photocatalytic Hydrogen Production of the Polyoxoniobate Modified with RGO and PPy

Shiliang Heng¹, Lei Li^{1,2}, Weiwei Li¹, Haiyan Li¹, Jingyu Pang¹, Mengzhen Zhang¹, Yan Bai^{1,*} and Dongbin Dang^{1,*}

¹ Henan Key Laboratory of Polyoxometalate Chemistry, College of Chemistry and Chemical Engineering, Henan University, Kaifeng 475004, China; 104753170767@vip.henu.edu.cn (S.H.); leili1202@126.com (L.L.); 104753160776@vip.henu.edu.cn (W.L.); lihaiyan@henu.edu.cn (H.L.); pjy@henu.edu.cn (J.P.); 104754181031@vip.henu.edu.cn (M.Z.)

² College of Chemistry and Chemical Engineering, Anyang Normal University, Anyang 455002, China

* Correspondence: baiyan@henu.edu.cn (Y.B.); dangdb@henu.edu.cn (D.D.)

Received: 27 October 2020; Accepted: 2 December 2020; Published: 7 December 2020



Abstract: The development of high-efficiency, recyclable, and inexpensive photocatalysts for water splitting for hydrogen production is of great significance to the application of solar energy. Herein, a series of graphene-decorated polyoxoniobate photocatalysts Nb₆/PPy-RGO (Nb₆ = K₇HNb₆O₁₉, RGO = reduced graphene oxide, PPy = polypyrrole), with the bridging effect of polypyrrole were prepared through a simple one-step solvothermal method, which is the first example of polyoxoniobate-graphene-based nanocomposites. The as-fabricated photocatalyst showed a photocatalytic H₂ evolution activity without any co-catalyst. The rate of 1038 μmol g⁻¹ in 5 h under optimal condition is almost 43 times higher than that of pure K₇HNb₆O₁₉·13H₂O. The influencing factors for photocatalysts in photocatalytic hydrogen production under simulated sunlight were studied in detail and the feasible mechanism is presented in this paper. These results demonstrate that Nb₆O₁₉ acts as the main catalyst and electron donor, RGO provides active sites, and PPy acted as an electronic bridge to extend the lifetime of photo-generated carriers, which are crucial factors for photocatalytic H₂ production.

Keywords: polyoxoniobate; Nb₆/PPy-RGO composites; electronic bridge; H₂ production

1. Introduction

With the widespread energy consumption and environmental problems, it is necessary and urgent to search for sources of green and clean energy to replace traditional fossil fuels [1–4]. Since the first discovery of photoelectrochemical water splitting into H₂ via the semiconductor TiO₂ by Fujishima and Honda in 1972, photocatalytic water splitting to hydrogen production has long been viewed as a promising and attractive strategy [5]. In recent years, many semiconductor materials have been reported for photocatalytic hydrogen evolution, in which the band gap, the position of the conduction band, the separation of electrons and holes and the lifetime of carriers are the key factors affecting photocatalysis [6,7]. Nonetheless, the exploitation of highly effective semiconductor materials for photocatalytic hydrogen evolution is still in the infant stage [8–10].

Polyoxometalates (POMs) have been applied in photocatalytic H₂ or O₂ evolution and the photodegradation of organic dyes [11–16], due to their controllable and stable structures, superior redox and semiconductor properties [17–22]. However, the lower H₂ production rates and the introduction of the scarce noble metal have largely limited the scale of their potential applications. It is a feasible strategy to design and prepare photocatalyst composites based on POMs, such as [PW₁₂O₄₀]³⁻, [PMo₁₂O₄₀]³⁻, [SiW₁₂O₄₀]⁴⁻ and [PMo₁₀V₂O₄₀]⁵⁻ [23–30]. In 2018, Zhang reported an interesting

investigation on the preparation of a novel $\text{Ag}_3\text{PO}_4/\text{POM}/\text{graphene oxide (GO)}$ heterostructure photocatalyst based on molybdophosphoric acid, which has excellent photocatalytic activity for photodegraded rhodamine B and water splitting for H_2 evolution, because of its increased surface area, electronegativity and structural stability [28]. This is a pioneering work in the study of photocatalyst composites from well conductive graphene and POMs for H_2 production.

Graphene is an ideal support material and as a solid electron mediator in photocatalysis, owing to the special 2D sp^2 -hybridized honeycomb structure [2,31], high charge carrier mobility (ca. $10,000 \text{ cm}^2 \text{ V}^{-1} \text{ s}^{-1}$) and large theoretical surface area ($2600 \text{ m}^2 \text{ g}^{-1}$) [32–34]. Therefore, the combination of graphene with semiconductors can not only inhibit the recombination of the photogenerated electron-hole pairs, but also adjust the band gap of photocatalysts and provide more photoactive sites [35–37]. More importantly, functionalization of N-doped graphene is a good way to improve the photocatalytic behavior. In particular, pyrrole-N-doped graphene is used as an oxygen-reduction active site to accelerate the interface-catalytic process [38]. Therefore, it is a promising work to introduce pyrrole into POM and graphene-based composites for photocatalytic decomposition of water into H_2O_2 or hydrogen and oxygen.

As an important kind of POMs, polyoxoniobates have been widely used in photocatalytic H_2 evolution due to higher negative charges and stronger basicity of $[\text{Nb}_6\text{O}_{19}]^{8-}$, which can easily accept electrons and keep an intact structure. Recently, several studies on photocatalytic H_2 evolution by polyoxoniobates have been reported, in which precious metals are essential components as co-catalysts [39–43]. Taking these studies into account, we hope to design a new type of POM-based composite photocatalysts with good photocatalytic H_2 production performance without any co-catalyst. Therefore, graphene was introduced into $[\text{Nb}_6\text{O}_{19}]^{8-}$ for the first time to produce composite photocatalysts, where it could act as the active sites to produce H_2 , avoiding the use of the scarce noble metal, while using economical and non-toxic pyrrole as a bridging material to prolong the lifetime of photo-generated carriers [44,45], decreasing the recombination of electron-hole pairs. Herein, $\text{Nb}_6/\text{PPy-RGO}$ ($\text{Nb}_6 = \text{K}_7\text{HNb}_6\text{O}_{19}$, RGO = reduced graphene oxide, PPy = polypyrrole), composites with the appearance of peony flowers were prepared using a simple one-pot solvothermal process. By adjusting the molar rate of Nb_6 , the volume of pyrrole and solvothermal temperature, a series of $\text{Nb}_6/\text{PPy-RGO}$ nanocomposites were obtained. Among the achieved $\text{Nb}_6/\text{PPy-RGO}$ composites, $\text{Nb}_6/\text{PPy-RGO-0.25}$ shows an outstanding photocatalytic activity with H_2 production rate of $1038 \mu\text{mol g}^{-1}$ in 5 h under the simulated sunlight without co-catalyst. Moreover, as-obtained $\text{Nb}_6/\text{PPy-RGO}$ composites demonstrate high stability and superb recyclability, which can be attributed to the collaborations among Nb_6 , RGO and PPy.

2. Materials and Methods

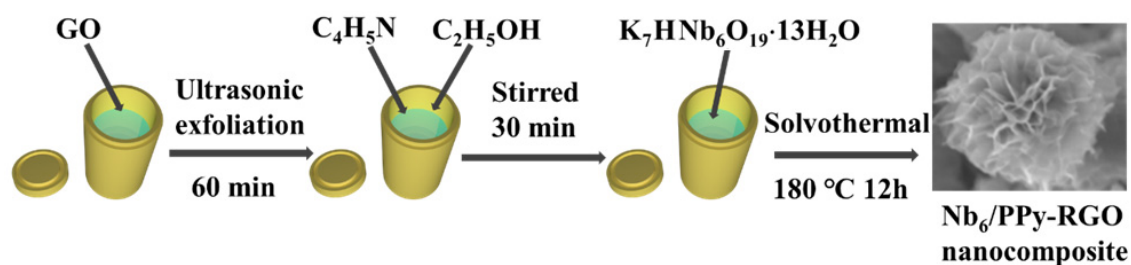
2.1. Materials

All the reagents and solvents used in this experiment were reagent grade and were used without further treatment. Graphite powder, sulfuric acid (H_2SO_4 , 98%), sodium sulfate (Na_2SO_4 , 99%), sodium nitrate (NaNO_3 , 99%), potassium permanganate (KMnO_4 , 99.5%) and pyrrole ($\text{C}_4\text{H}_5\text{N}$, 98%) were purchased from Aladdin Biochemical Technology Co. (Shanghai, China). The $\text{K}_7\text{HNb}_6\text{O}_{19} \cdot 13\text{H}_2\text{O}$ was synthesized according to the method in the literature [46], and its purity was determined by infrared spectra (IR). Graphene oxide (GO) was manufactured by a modified Hummers' method and the purity of GO was confirmed by X-ray diffraction (XRD) [47,48].

2.2. Synthesis of $\text{Nb}_6/\text{PPy-RGO}$

As shown in Scheme 1, 4 mg graphene oxide (GO) was added to 2 mL distilled water in a 25 mL Teflon lining and ultrasonic for 1 h. Then, a solution containing 110 μL pyrrole (denoted as Py) and 1 mL ethanol was added to the above solution. After stirring for 30 min, Nb_6 (345 mg, 0.25 mmol) was added to the mixed solution and heated at 180°C for 12 h. After cooling to room temperature, the achieved product, $\text{Nb}_6/\text{PPy-RGO-0.25}$, was respectively washed with deionized water four times

and ethanol two times to remove the excess reactants, and finally dried at 60 °C under vacuum for 12 h. According to the same procedure, except for the amount of Nb₆ (173 mg, 0.125 mmol) and (523 mg, 0.375 mmol), the samples Nb₆/PPy-RGO-0.125 and Nb₆/PPy-RGO-0.375 were respectively obtained. Similarly, to gain further insight into the effect of the amount of Nb₆ and reaction temperature on the photocatalytic activity of the catalysts, controlling the amount of Nb₆ (0.25 mmol), GO and temperature, we achieved Nb₆/PPy-RGO-90 and Nb₆/PPy-RGO-130 by adjusting the amount of pyrrole (90 and 130 μL). Simultaneously, controlling the amount of Nb₆ (0.25 mmol), GO and pyrrole (110 μL), the samples Nb₆/PPy-RGO-160 °C and Nb₆/PPy-RGO-190 °C were fabricated. As a comparison, the PPy-RGO was also obtained without the addition of Nb₆.



Scheme 1. Illustration of the synthesis process of Nb₆/PPy-RGO composites (K₇HNb₆O₁₉·13H₂O = Nb₆, RGO = reduced graphene oxide, PPy = polypyrrole).

2.3. Characterization

The morphology and microstructure of the synthetic samples were characterized using a field emission scanning electron microscopy (FESEM, JSM-7610F, Electronics Co., LTD., Tokyo, Japan) at 10 kV and a transmission electron microscopy (TEM, JEM-2100F, Electronics Co., LTD., Tokyo, Japan) at 200 kV. Powder X-ray diffraction (XRD, Bruker optics Instruments company, Karlsruhe, Germany) was measured from 5° to 80° at room temperature on a Bruker D8 Advance diffractometer with Cu-Kα radiation and the Fourier transform-infrared spectra (FT-IR, KBr pellets, Bruker optics Instruments company, Karlsruhe, Germany) were recorded on a Nicolet 170 SXFT-IR spectrophotometer ranging from 4000 to 500 cm⁻¹. X-ray photoelectron spectroscopy (XPS, Thermo Fisher Scientific, Waltham, MA, USA) was recorded on an ESCALAB 250Xi X-ray photoelectron spectrometer with an Al-Kα ($h\nu = 1486.6$ eV) monochromatic radiation source. The binding energy peak position of each sample was calibrated by the C 1s peak at 284.8 eV. UV-visible spectra were achieved on a Shimadzu UV-2600 UV/Vis spectrophotometer (Shimadzu Instrument Co., LTD, Kyoto-fu, Japan) using BaSO₄ as a reference. Raman spectroscopy (Renishaw company, London, UK) was prepared using a Renishaw in Via Raman spectrometer with excitation by 325 nm Photoluminescence (PL) spectra were obtained at excitation wavelength 385 nm with TU-1900 (PuXi Company, Beijing, China).

2.4. Photocatalytic Hydrogen Production

Photocatalytic hydrogen producing experiments were performed using a method similar to the literature [6]. Photocatalyst (50 mg) was added to a solution of deionized water (40.0 mL) and CH₃OH (10.0 mL, pH = 7) in a quartz vessel. The reaction system was irradiated by a 300 W Xe lamp (Perfect light PLS-SXE300, Perfectlight Technology Co., Ltd, Beijing, China), and the temperature was maintained at about 5 °C. The product H₂ was measured by gas chromatograph (FL-9790) on line. After each photocatalytic test, photocatalysts were collected by centrifugation without reactivated before each cycle, washed with H₂O and C₂H₅OH to remove impurities, then used after drying.

2.5. Photocatalytic Measurement

The Mott-Schottky curves were tested on an AMETEK Princeton Applied Research (Versa STAT 4, Princeton, NJ, USA) electrochemical workstation (FTO = fluorine-doped tin oxide substrate, 1 cm × 1.5 cm). The electrochemical impedance spectroscopy (EIS) and photocurrent response

were recorded on an electrochemical workstation (CHI660, Chenhua, Shanghai, China) equipped with a three-electrode system with a complex/FTO as the working electrode, platinum foil as the counter electrode and Ag/AgCl as the reference electrode in 0.2 M sodium sulfate solution (Na_2SO_4). The working electrode complex/FTO was prepared by dropwise adding 50 μL of sample suspensions containing $\text{Nb}_6/\text{PPy-RGO}$ composites (3.0 mg), ethanol (1.0 mL), and nafion (20 μL) onto a FTO substrate (1 cm \times 1.5 cm).

3. Results and Discussion

3.1. Structural Characterizations

The XRD patterns of GO, Nb_6 , and $\text{Nb}_6/\text{PPy-RGO}$ composites were investigated. As shown in Figure 1 and Figure S1, pristine GO and RGO show a single peak near 12° and 26° , respectively, while pristine $\text{K}_7\text{HNb}_6\text{O}_{19}$ has sharp diffraction peaks at 9.7° , 26° and 48° , respectively, which is consistent with the literature reports [46–48]. The broad peaks centered on 27.5° of $\text{Nb}_6/\text{PPy-RGO}$ composites can be attributed to the combined action of PPy and RGO, while the characteristic peaks at 46° are attributed to the superposition of Nb_6 and PPy [49–51]. In $\text{Nb}_6/\text{PPy-RGO}$ composite materials, although it is not obvious in $\text{Nb}_6/\text{PPy-RGO-0.325}$ and $\text{Nb}_6/\text{PPy-RGO-0.25}$, the characteristic peaks of raw materials can still be found. No additional diffraction peaks were observed, confirming the formation of the $\text{Nb}_6/\text{PPy-RGO}$ composites. The crystallite sizes of the catalysts calculated from the XRD patterns were shown in Table 1.

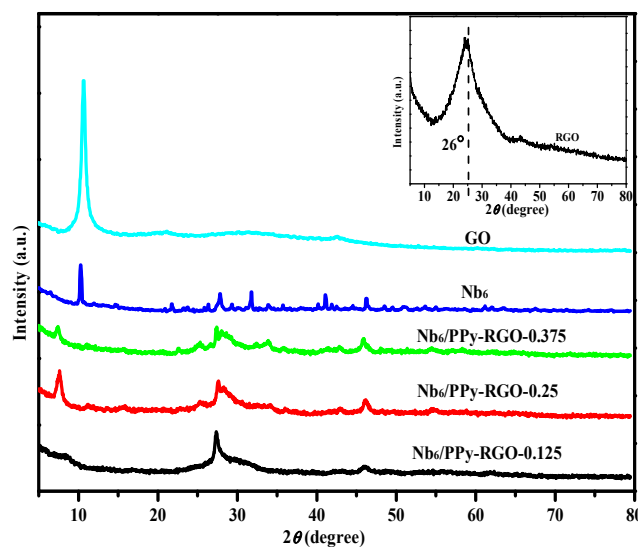


Figure 1. X-ray diffraction (XRD) patterns of graphene oxide (GO), RGO (insert figure), Nb_6 and $\text{Nb}_6/\text{PPy-RGO}$ composites.

Table 1. The crystallite sizes of Nb_6 and $\text{Nb}_6/\text{PPy-RGO}$ composites ($\text{Nb}_6 = \text{K}_7\text{HNb}_6\text{O}_{19}$, RGO = reduced graphene oxide, PPy = polypyrrole).

Samples	Nb_6	$\text{Nb}_6/\text{PPy-RGO-0.125}$	$\text{Nb}_6/\text{PPy-RGO-0.25}$	$\text{Nb}_6/\text{PPy-RGO-0.375}$
Crystallite sizes (nm)	26	6	12	14

The structure of $\text{Nb}_6/\text{PPy-RGO-0.25}$ composite has also been evidenced by Fourier transform-infrared (FT-IR) spectroscopy (Figure 2). The peak at 1398 cm^{-1} is assigned to the C-O stretching vibration due to π - π interaction between PPy and RGO. The peak at 1637 cm^{-1} is assigned to H-O-H stretching vibration and the peak at 1258 cm^{-1} was assigned to C-H and C-N in-plane deformation vibration, further implying the combination of GO with PPy [52,53]. The characteristic peaks at 840 and 887 cm^{-1} could be attributed to the terminal Nb-O stretching vibration, and the peaks

appearing at 532 and 597 cm^{-1} correspond to Nb-O-Nb bonds [54]. The result shows that Nb₆ was successfully inserted into the final composite.

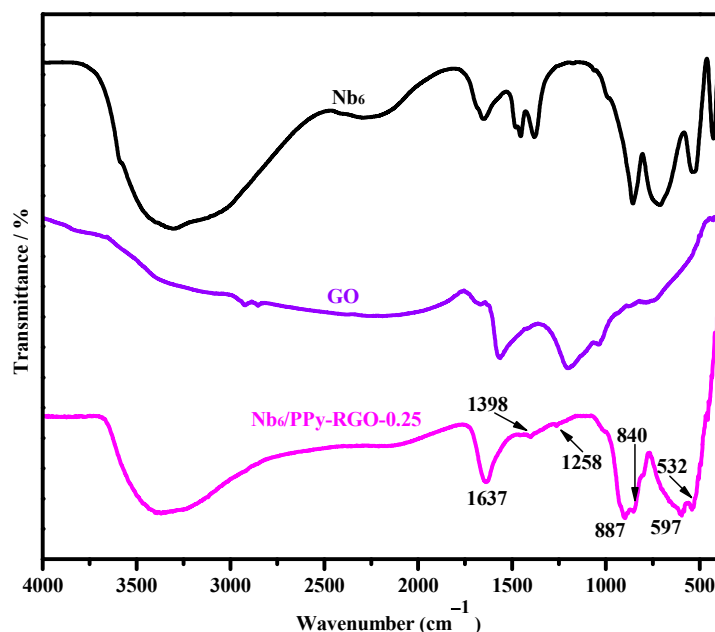


Figure 2. Fourier transform-infrared (FT-IR) spectra of Nb₆, GO and Nb₆/PPy-RGO-0.25.

From the Raman spectra shown in Figure 3, the higher wavenumber bands at 1334 and 1584 cm^{-1} are ascribed to D band and G band of GO. It is worth noting that the peak intensity ratio (I_D/I_G) is a popular method to evaluate the disorder and reduction of graphene materials. The I_D/I_G ratio of the pure GO is about 0.76, while that of the Nb₆/PPy-RGO-0.25 composite is about 0.99. The numeric addition indicated that the oxygen-containing functional groups were partially reduced, meaning the transition of GO to RGO in the process of solvothermal reaction [54]. Compared with the characteristic peaks of Nb₆ (541, 827 and 875 cm^{-1}) [55,56], the redshift could be found for Nb₆/PPy-RGO-0.25 (878 and 620 cm^{-1}), which may be assigned to the strong interaction among the Nb₆, PPy, and RGO of the composites.

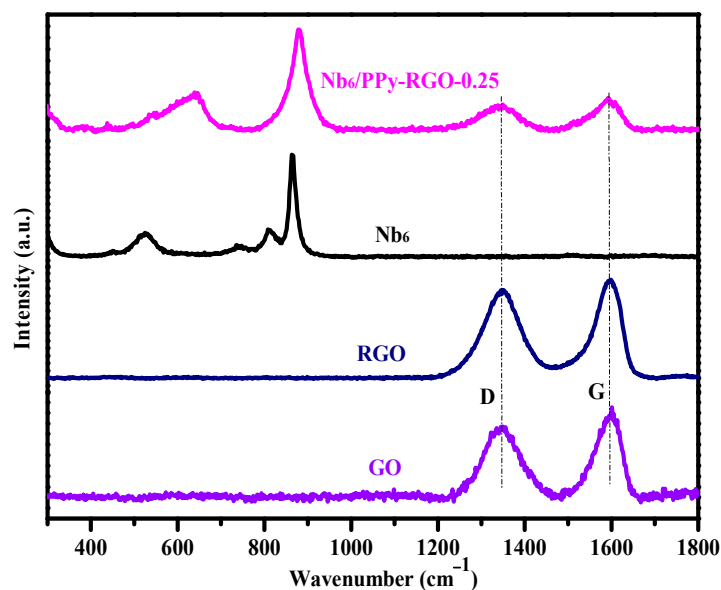


Figure 3. Raman spectra of Nb₆, GO, RGO and Nb₆/PPy-RGO-0.25.

In order to further identify the structure of composites, the XPS spectra were tested for Nb₆/PPy-RGO-0.25 composites and GO, as well as Nb₆ (Figure 4). As shown in Figure 4A, the full spectrum clearly shows the presence of C, O, N, K, and Nb elements in the composite sample, which is consistent with the chemical composition of the photocatalyst. As shown in Figure 4B, the binding energies of C 1s, including 284.05, 285.60, 286.47 and 288.37 eV, could be attributed to carbon of the non-oxygenated ring, C-OH, C-O and C=O in Nb₆/PPy-RGO-0.25, respectively, which are lower and weaker than that of pure GO (284.74, 285.97, 287.07 and 289.08 eV). These results demonstrate that the GO has been successfully reduced in composites, which is in agreement with Raman spectra [57–60]. For pure GO, the XPS of O 1s contains two peaks at 532.20 and 533.08 eV assigned to C=O/C-O and O-C=O, respectively. The peaks at 531.96, 529.05, and 530.63 eV in the pure Nb₆ sample belong to Nb-O-Nb, Nb-O-H, and crystal water, respectively. There are two main peaks at 529.73 and 531.74 eV in Nb₆/PPy-RGO-0.25, which can be attributed to binding energies of O 1s in Nb-O-Nb and Nb-O-H (Figure 4C [61]). Figure 4D illustrates a comprehensive Nb 3d XPS analysis of the Nb₆/PPy-RGO-0.25 and Nb₆. The binding energies of 206.49 and 209.26 eV could be assigned to Nb 3d_{5/2} and Nb 3d_{3/2} of Nb⁵⁺ (highest oxidation state) in Nb₆/PPy-RGO-0.25. Compared with Nb₆, the peaks of Nb 3d shifted to higher binding energy by ~1 eV, which may be caused by electron transfer from Nb₆ to RGO in composites [54]. As shown in Figure 4E, the N 1s peaks centered at 398.01 and 399.55 eV are vested to the pyridinic and pyrrolic of N atom in polymer. In addition, there is a weak peak at the center of 394.11 eV, corresponding to the Nb-N bond, indicating the formation of chemical bonds between PPy and Nb₆ [62].

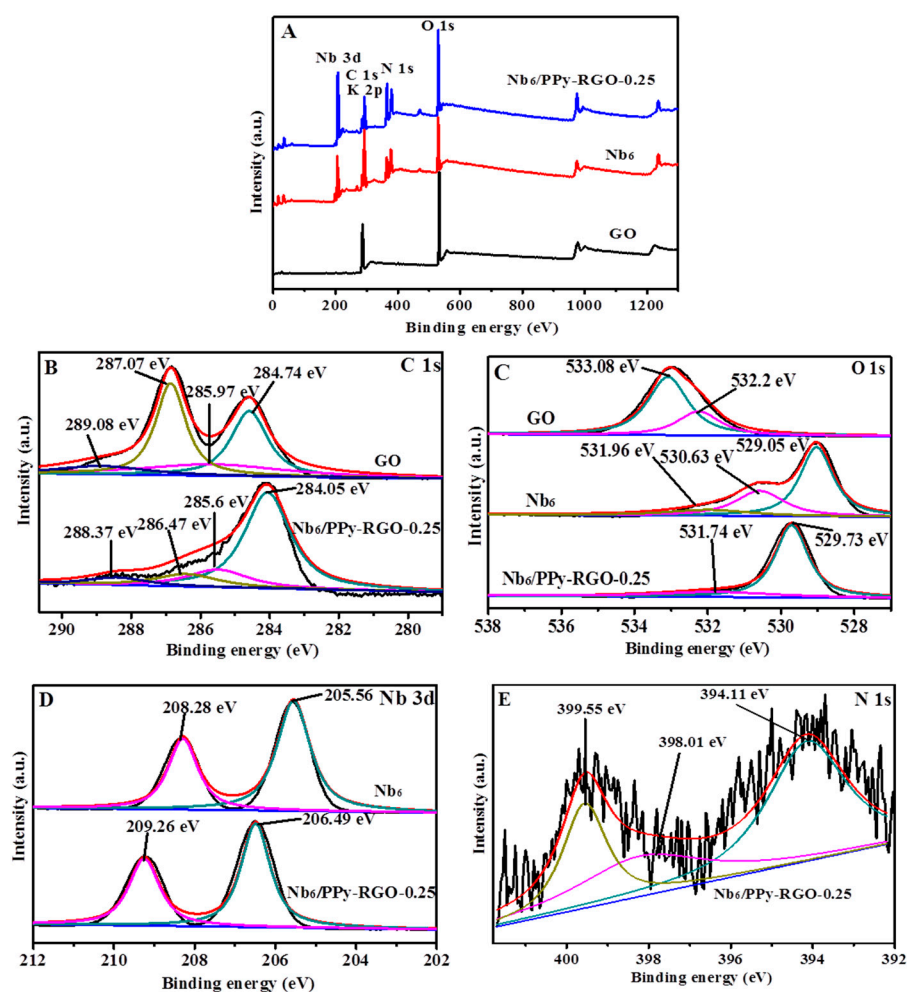


Figure 4. X-ray photoelectron spectroscopy (XPS) of GO, Nb₆, and Nb₆/PPy-RGO-0.25, (A) survey; (B) C 1s; (C) O 1s; (D) Nb 3d; (E) N 1s.

3.2. Nanosphere Morphologies

As shown in Figure 5, the results show that the morphology of Nb₆ is rodlike. However, when fabricated with PPy and RGO, Nb₆/PPy-RGO-X (X = 0.125, 0.25, 0.375) display the flower-like methodology. To deeply understand the formation of flower-like methodology, the controlled experiments including solvothermal reaction temperatures and the amount of Py have been respectively conducted using Nb₆/PPy-RGO-0.25 as a representative. As shown in Figures S2 and S3, the samples probably agglomerated when changing the conditions of 160 °C or Py (130 μL). However, the lower amount of Py, with 90 μL, or higher temperature of 190 °C may reduce the surface area and could not form morphology of flowers for Nb₆/PPy-RGO-0.25. These results demonstrate that the flower-like morphology for Nb₆/PPy-RGO-0.25 largely depends on the temperature and the amounts of Py in the reaction. The corresponding EDS elemental mapping of Nb₆/PPy-RGO-0.25 indicated the elements of C, N, O, K and Nb were uniformly distributed throughout the whole composite (Figure 5E).

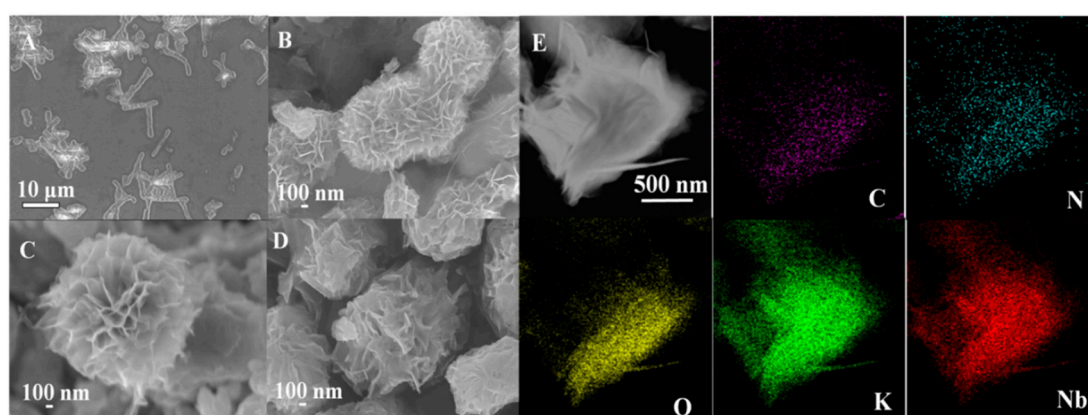


Figure 5. Scanning electron microscopy (SEM) images for: (A) Nb₆; (B) Nb₆/PPy-RGO-0.125; (C) Nb₆/PPy-RGO-0.25; (D) Nb₆/PPy-RGO-0.375. (E) Transmission electron microscopy (TEM) images and the element maps of Nb₆/PPy-RGO-0.25.

3.3. Photochemistry and Electrochemistry

The UV-Vis diffuse reflectance spectra of Nb₆/PPy-RGO composites were recorded at room temperature to discuss their optical properties, together with Nb₆ for comparison. As shown in Figure 6, Nb₆/PPy-RGO composites exhibit broad absorptions in the range of 200–340 nm. Compared with the absorption of Nb₆ (200–315 nm), the light absorption of Nb₆/PPy-RGO samples was obviously widened, which is related to the introduction of PPy and RGO. Due to the zero band gap for RGO, with the increasing amounts of Nb₆, the absorbance intensity for Nb₆/PPy-RGO composites become weaker (Figure 6a). Simultaneously, the color becomes lighter and the ability to capture light is decreased (Figure S4), hinting that the enhanced absorption is mainly attributed to the introduction of RGO. The band-gap values of Nb₆ and Nb₆/PPy-RGO composites (from 0.125 to 0.375) obtained by the Kubelka–Munk function via the UV-Vis diffuse reflectance are 4.14, 3.66, 3.71, and 3.76 eV, respectively, indicating the semiconductor characters of Nb₆/PPy-RGO composites (Figure 6b). Compared to the band gap value of Nb₆, those of Nb₆/PPy-RGO composites are obviously narrowed through the incorporation of RGO and PPy.

Furthermore, the potentials of conduction band (CB) of Nb₆/PPy-RGO composites could be obtained from electrochemical Mott–Schottky plots (Figure S5). The plots of C⁻² vs. potential exhibited positive slopes, indicating that we should consider the composites as typical n-type semiconductors [57]. The flat band position of Nb₆/PPy-RGO composites determined from the intersection of the Mott–Schottky plot and X axis are approximately −1.01 V (Nb₆/PPy-RGO-0.125), −1.34 V (Nb₆/PPy-RGO-0.25) and −1.23 V (Nb₆/PPy-RGO-0.375) (vs. NHE, NHE = Normal hydrogen electrode). These results imply that the potentials of CB of Nb₆/PPy-RGO composites are more negative

than the redox potential of H^+/H_2 (-0.41 V vs. NHE, pH = 7) [63], indicating the title composites should be used as photocatalysts for hydrogen evolution via water splitting.

As shown in Figure S6, compared with other composites, the $Nb_6/PPy-RGO-0.25$ composite displays the weakest PL intensity at 378 nm, and the amount of pyrrole and the solvothermal temperature had little effect on the separation of photo-excited charge and holes, indicative of the lowest combination of electron-hole pairs. Because $K_7HNb_6O_{19}$ has good water solubility, electrochemical measurement cannot be performed under the same conditions. As shown in Figure 7a, the highest photocurrent response of $Nb_6/PPy-RGO-0.25$ shows better separation ability and lower recombination of photogenerated electron-hole pairs [42]. As depicted in Figure 7b, the smallest radius of $Nb_6/PPy-RGO-0.25$ indicates lower charge transfer resistance. This result confirms that more photo-generated charge carriers can be separated by constructing $Nb_6/PPy-RGO-0.25$, which is consistent with the result of PL analysis and photocurrent response.

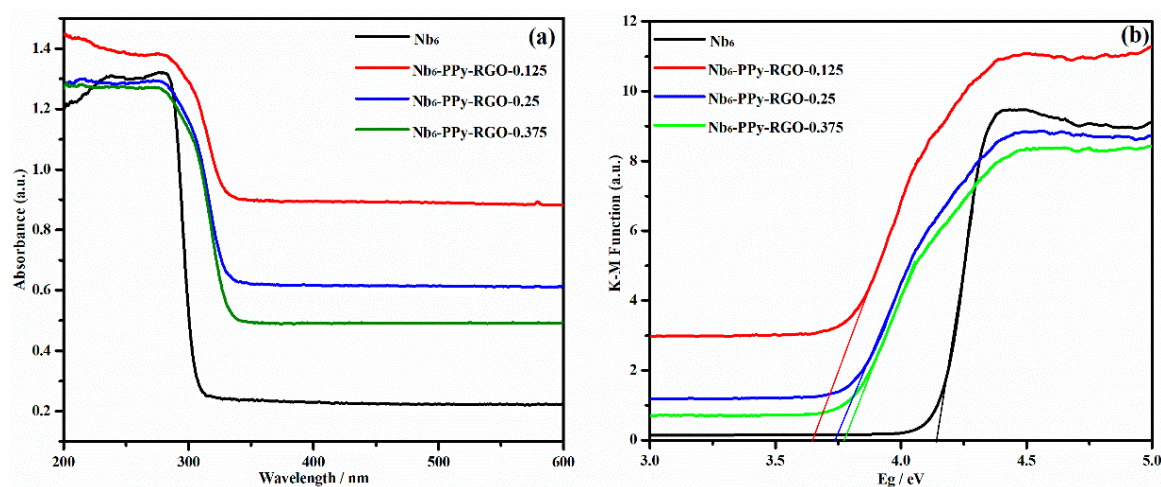


Figure 6. (a) UV-vis diffuse reflectance spectra of Nb_6 and $Nb_6/PPy-RGO$ composites; (b) Kubelka-Munk function-calculated band gap of Nb_6 and $Nb_6/PPy-RGO$ composites.

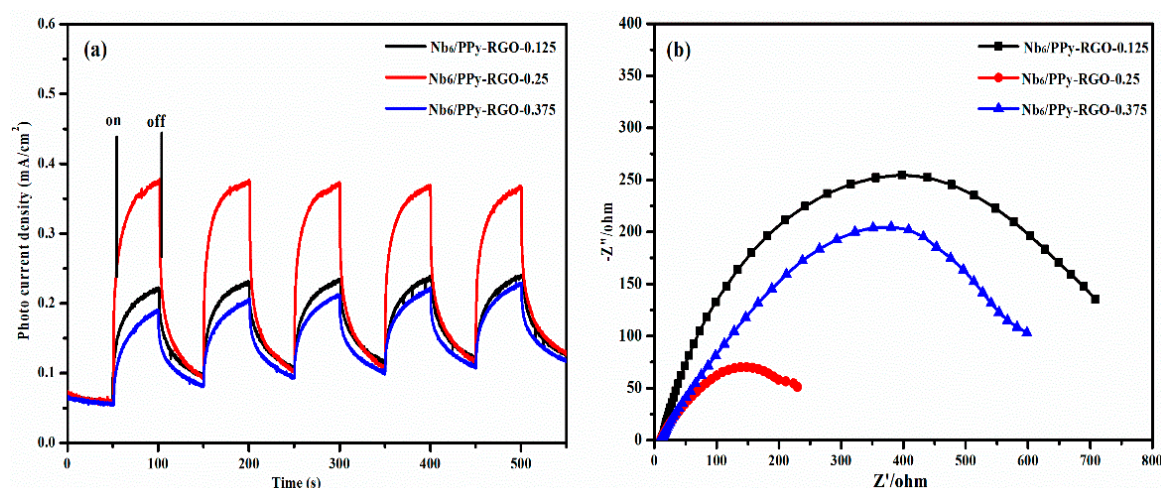


Figure 7. (a) Transient photocurrent response and (b) electrochemical impedance spectroscopy (EIS) plots of $Nb_6/PPy-RGO-0.125$, $Nb_6/PPy-RGO-0.25$ and $Nb_6/PPy-RGO-0.375$.

3.4. Photocatalytic Hydrogen Evolution

Photocatalytic activity of $Nb_6/PPy-RGO$ composites for hydrogen evolution via water splitting was evaluated in aqueous solution with methanol (CH_3OH) as a sacrificial electron donor. As shown in Figure 8, the H_2 production for $Nb_6/PPy-RGO$ composites was 351.5 ($Nb_6/PPy-RGO-0.125$), 1038 ($Nb_6/PPy-RGO-0.25$) and 690.5 $\mu mol g^{-1}$ ($Nb_6/PPy-RGO-0.375$) in 5 h, respectively. Under the

same conditions, the H₂ production was 25 μmol g⁻¹ for the Nb₆ catalyst. Apparently, the composites exhibit higher photocatalytic activity by introduction of PPy and RGO. Compared with the other two composites, Nb₆/PPy-RGO-0.125 and Nb₆/PPy-RGO-0.375, Nb₆/PPy-RGO-0.25 exhibits better photocatalytic efficiency and the turnover frequency (TOF) value reaches 830.4 × 10⁻³ h⁻¹ (Table 2). These results agree well with EIS and photo-current measurements.

Turnover frequency (TOF) was based on Nb₆, which has been widely used to evaluate the property of catalysts, especially for POM-based catalysts. The details are as follows:

$$\text{TOF} = \frac{n_{(\text{H}_2)}/\text{h}}{n_{(\text{Nb}_6)}} \quad (1)$$

Taking Nb₆/PPy-RGO-0.25 as an example:

$$\text{TOF}_{(\text{Nb}_6/\text{PPy-RGO-0.25})} = \frac{n_{(\text{H}_2)}/\text{h}}{n_{(\text{Nb}_6)}} = \frac{1038 \times 10^{-6} \text{ mol}/5\text{h}}{0.25 \times 10^{-3} \text{ mol}} = 830.4 \times 10^{-3} \text{ h}^{-1} \quad (2)$$

Table 2. The turnover frequency (TOF) values of Nb₆ and Nb₆/PPy-RGO composites.

Samples	Nb ₆	Nb ₆ /PPy-RGO-0.125	Nb ₆ /PPy-RGO-0.25	Nb ₆ /PPy-RGO-0.375
TOF (h ⁻¹)	137 × 10 ⁻³	562.6 × 10 ⁻³	830.4 × 10 ⁻³	368 × 10 ⁻³

From the above table, the sample Nb₆/PPy-RGO-0.25 showed the better photocatalytic activity.

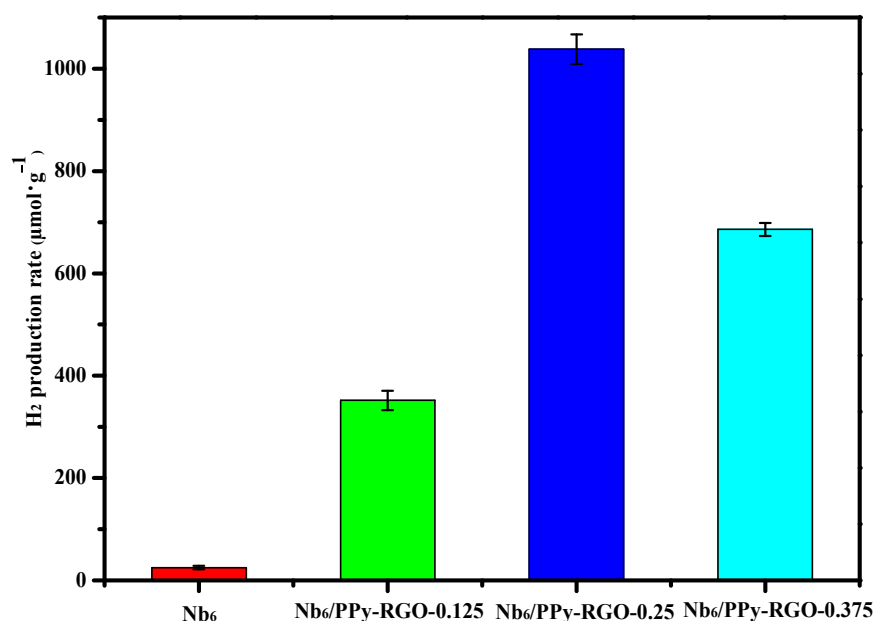


Figure 8. Hydrogen evolution of Nb₆ and Nb₆/PPy-RGO composites in aqueous solution with MeOH 20%.

The photocatalytic system has also been optimized by changing the amount or species of sacrificial electron donors by using the optimal as Nb₆/PPy-RGO-0.25 photocatalyst. As shown in Figure S7a, when the concentration of CH₃OH increased from 0 to 20% (v:v), the hydrogen evolution increased from 0 to 1038 μmol g⁻¹, but decreased to 274 and 94 μmol g⁻¹ with higher concentrations of 25% (v:v) and 30% (v:v), respectively. These results imply that the amount of CH₃OH played an important role in photocatalytic hydrogen evolution. The more sacrificial electron donors may react with holes of photocatalyst to release more photo-excited electrons to produce more hydrogen. However, with an excess of CH₃OH, it should also decrease the concentrations of substrate, leading to lower

photocatalytic efficiency. Furthermore, the species of sacrificial electron donor was optimized by controlling the ratio of sacrificial agent/H₂O (*v:v* = 10:40) (Figure S7b). The title photocatalyst exhibited the optimal H₂ production of 1038 μmol g⁻¹ with CH₃OH as the sacrificial agent, but varied in the range of 249.5–834 μmol g⁻¹ with other sacrificial agents. As shown in Figure S8, the best sample, Nb₆/PPy-RGO-0.25, exhibits the highest photocatalytic H₂ production, indicating the optimal reaction conditions with pyrrole dosage of 110 μL and reaction temperature of 180 °C.

In order to prove the reusability of Nb₆/PPy-RGO-0.25, the recycling experiment was carried out (Figure 9). There was no noticeable deactivation observed for the catalyst and the yields of H₂ evolution for the four recycling experiments all remained at 1000 μmol g⁻¹ in 5 h. In addition, the XRD pattern (Figure S9), Raman spectra (Figure S10) and SEM image (Figure S11) of the recovered catalysts were alike to those of the as-prepared sample, further demonstrating the recyclability and stability of Nb₆/PPy-RGO-0.25 in the photocatalysis reaction.

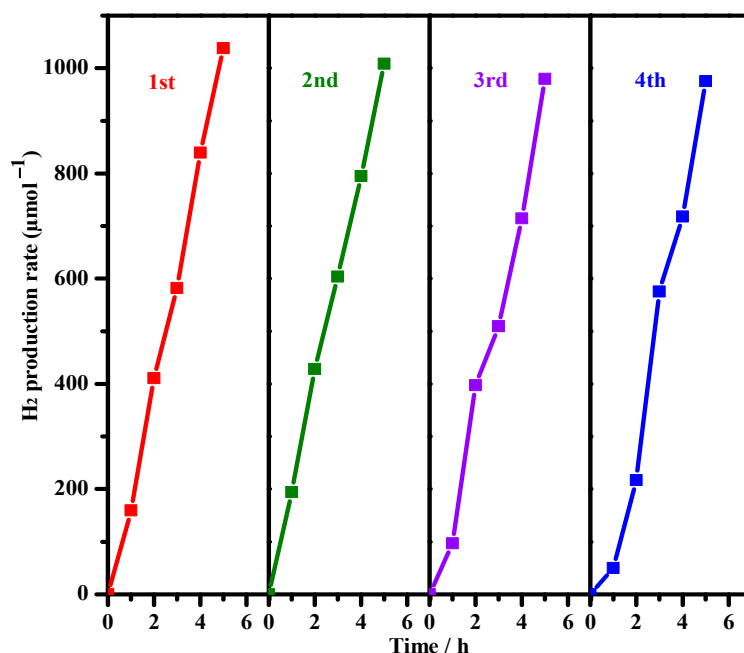


Figure 9. Changes in photocatalytic performance of Nb₆/PPy-RGO-0.25 during the recycled uses.

3.5. Proposed Photocatalytic Mechanism

According to the Mott–Schottky plot shown in Figure S5, the conduction band minimum (CBM) of the composites could be estimated to explain the enhanced photocatalytic activity mechanism, which is about -1.34 eV for the sample Nb₆/PPy-RGO-0.25 possessing the best H₂ evolution performance. Meanwhile, valence band maximum (VBM) potential of Nb₆/PPy-RGO-0.25 can be determined based on the formula $E_{\text{VBM}} = E_{\text{CBM}} + E_g$, which is about 2.37 eV [64]. As displayed in Figure 10, the pure Nb₆ exhibits negligible photocatalytic activity, which may be due to the fast recombination of electrons and holes. Higher photocatalytic efficiency can be achieved for Nb₆/PPy-RGO composites by the modification with PPy and RGO. It has been reported that conductive polymers can be used as photocatalysts for H₂ production from water splitting [65]. However, in such Nb₆/PPy-RGO-0.25 composites, pure PPy and RGO cannot exhibit photocatalytic activity due to their combination of electrons and holes. On the other hand, they can prolong the lifetime of charge carriers to promote the separation efficiency of electron-hole pairs in Nb₆/PPy-RGO-0.25 composites due to their excellent π conjugated chain structure and electrical conductivity. In addition, RGO can also serve as active sites to produce H₂, avoiding the use of noble metals, while PPy acted as conductive polymers, promoting the transfer of the electrons [52,53,66–69]. In particular, the π - π interaction between RGO and PPy further strengthens the electrical conductivity. Based on the above results, a probable photocatalytic

mechanism for composites could be proposed as follows: under light irradiation, the electrons in the valence band (VB) of Nb₆/PPy-RGO-0.25 can be excited to the CB, causing holes in the VB. On one hand, the holes in the VB could be quenched by accepting electrons from CH₃OH. On the other hand, the photoelectron in the CB of Nb₆/PPy-RGO-0.25 could be transferred to RGO through the bridge of PPy. Acting as photoactive sites, the RGO accepting electrons would react with H₂O to produce H₂.

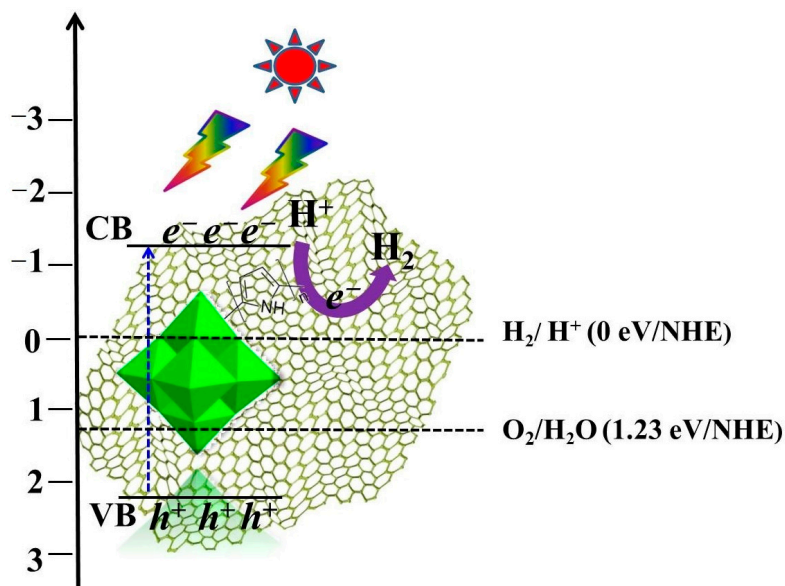


Figure 10. The proposed photocatalytic hydrogen production mechanism of Nb₆/PPy-RGO-0.25 (NHE = normal hydrogen electrode).

4. Conclusions

In summary, a series of unprecedented polyoxoniobate-graphene nanocomposites, Nb₆/PPy-RGO, have been successfully synthesized through a simple one-step solvothermal method. This is the first example of polyoxoniobate-graphene nanocomposites for photocatalytic H₂ production. This work presents a new idea for the design and synthesis of high-performance polyoxometalates-graphene photocatalysts in photocatalytic H₂ production. Nb₆/PPy-RGO was optimized by adjusting the amount of Nb₆, volume of pyrrole and temperature, displaying superb photocatalytic H₂ production of 1038 μmol g⁻¹ in 5 h without a co-catalyst, almost 43 times more than pure Nb₆, in which the collaborations among Nb₆, PPy and RGO play vital roles in such a photocatalytic system. In further work, we will focus on studying more fascinating polyoxoniobate-graphene nanocomposites with new interesting properties.

Supplementary Materials: The following are available online at <http://www.mdpi.com/2079-4991/10/12/2449/s1>, Figure S1: X-ray diffraction (XRD) patterns for series of concentration of pyrrole and temperature and the corresponding starting materials. Figure S2: SEM images for (a) Nb₆-RGO; (b) Nb₆/PPy-RGO-90 μL; (c) Nb₆/PPy-RGO-110 μL; (d) Nb₆/PPy-RGO-130 μL (SEM = scanning electron microscopy, Nb₆ = K₇HNb₆O₁₉, RGO = reduced graphene oxide, PPy = polypyrrole). Figure S3: SEM images for (a) Nb₆/PPy-RGO-160 °C; (b) Nb₆/PPy-RGO-180 °C; (c) Nb₆/PPy-RGO-190 °C. Figure S4: The color change of samples. Figure S5: Mott-Schottky plots of (a) Nb₆/PPy-RGO-0.125; (b) Nb₆/PPy-RGO-0.25; (c) Nb₆/PPy-RGO-0.375, in 0.2 M Na₂SO₄ aqueous solution with pH = 7. Figure S6: Photoluminescence (PL) spectra recorded at room temperature in the range of 325–450 nm with an excitation wavelength of 378 nm for adjust (a) molar ratio of Nb₆; (b) volume of pyrrole; (c) temperature. Figure S7: (a) Rate of H₂ evolution as a function of CH₃OH concentration, (b) Rate of H₂ evolution as a function of type of sacrificial agents. Figure S8: Photocatalytic hydrogen production in concentration of pyrrole (a) and temperature (b) in aqueous solution with MeOH 20%. Figure S9: XRD patterns of Nb₆/PPy-RGO-0.25 before and after photocatalytic H₂ evolution reaction. Figure S10: Raman spectra of Nb₆/PPy-RGO-0.25 before and after photocatalytic H₂ evolution reaction. Figure S11: SEM images for (a) Nb₆/PPy-RGO-0.25 and (b) that after the recycle of photocatalytic hydrogen evaluation.

Author Contributions: Conceptualization, S.H. and D.D.; investigation, S.H., W.L., H.L. and M.Z.; writing—original draft preparation, S.H. and L.L.; writing—review and editing, Y.B., D.D. and L.L.; supervision, Y.B. and D.D.; funding acquisition, Y.B. and J.P. All authors have read and agreed to the published version of the manuscript.

Funding: The author thanks the support of the National Natural Science Foundation of China (No. 21971055), the Foundation of the Education Department of Henan Province of China (No. 21A150011 and No. 19B150001), the Postdoctoral Science Foundation of China (No. 2019M652518), and the Postdoctoral Scientific Research Foundation of Henan Province.

Conflicts of Interest: The authors declare no conflict of interest.

References

1. Li, H.; Sun, Y.; Yuan, Z.Y.; Zhu, Y.P.; Ma, T.Y. Titanium Phosphonate Based Metal-Organic Frameworks with Hierarchical Porosity for Enhanced Photocatalytic Hydrogen Evolution. *Angew. Chem. Int. Ed.* **2018**, *57*, 3222–3227. [[CrossRef](#)] [[PubMed](#)]
2. Li, X.; Yu, J.G.; Wageh, S.; Al-Ghamdi, A.A.; Xie, J. Graphene in Photocatalysis: A Review. *Small* **2016**, *12*, 6640–6696. [[CrossRef](#)]
3. Zhang, G.; Wang, G.; Liu, Y.; Liu, H.; Qu, J.; Li, J. Highly Active and Stable Catalysts of Phytic Acid-Derivative Transition Metal Phosphides for Full Water Splitting. *J. Am. Chem. Soc.* **2016**, *138*, 14686–14693. [[CrossRef](#)] [[PubMed](#)]
4. Gao, M.M.; Zhu, L.L.; Ong, W.L.; Wang, L.; Ho, G.W. Structural design of TiO₂-based photocatalyst for H₂ production and degradation applications. *Catal. Sci. Technol.* **2015**, *5*, 4703–4726. [[CrossRef](#)]
5. Fujishima, A.; Honda, K. Electrochemical Photolysis of Water at a Semiconductor Electrode. *Nature* **1972**, *238*, 37–38. [[CrossRef](#)]
6. Li, L.; Zhu, S.; Hao, R.; Wang, J.J.; Yang, E.C.; Zhao, X.J. Amino group promoted photocatalytic hydrogen evolution activity observed in two copper(ii)-based layered complexes. *Dalton Trans.* **2018**, *47*, 12726–12733. [[CrossRef](#)]
7. Zhao, X.X.; Feng, J.R.; Liu, J.W.; Lu, J.; Shi, W.; Yang, G.M.; Wang, G.C.; Feng, P.Y.; Cheng, P. Metal-Organic Framework-Derived ZnO/ZnS Heteronanostructures for Efficient Visible-Light-Driven Photocatalytic Hydrogen Production. *Adv. Sci.* **2018**, *5*, 1700590–1700598. [[CrossRef](#)]
8. Afroz, K.; Moniruddin, M.; Bakranov, N.; Kudaibergenov, S.; Nuraje, N. A heterojunction strategy to improve the visible light sensitive water splitting performance of photocatalytic materials. *J. Mater. Chem. A* **2018**, *6*, 21696–21718. [[CrossRef](#)]
9. Stroyuk, O.; Raevskaya, A.; Gaponik, N. Solar light harvesting with multinary metal chalcogenide nanocrystals. *Chem. Soc. Rev.* **2018**, *47*, 5354–5422. [[CrossRef](#)]
10. Kumar, P.; Boukherroub, R.; Shankar, K. Sunlight-driven water-splitting using two-dimensional carbon based semiconductors. *J. Mater. Chem. A* **2018**, *6*, 12876–12931. [[CrossRef](#)]
11. Li, S.J.; Liu, S.M.; Liu, S.X.; Liu, Y.W.; Tang, Q.; Shi, Z.; Ouyang, S.X.; Ye, J.H. {Ta₁₂}/{Ta₁₆} Cluster-Containing Polytantalotungstates with Remarkable Photocatalytic H₂ Evolution Activity. *J. Am. Chem. Soc.* **2012**, *134*, 19716–19721. [[CrossRef](#)] [[PubMed](#)]
12. Qin, J.S.; Du, D.Y.; Guan, W.; Bo, X.J.; Li, Y.F.; Guo, L.P.; Su, Z.M.; Wang, Y.Y.; Lan, Y.Q.; Zhou, H.C. Ultrastable Polymolybdate-Based Metal-Organic Frameworks as Highly Active Electrocatalysts for Hydrogen Generation from Water. *J. Am. Chem. Soc.* **2015**, *137*, 7169–7177. [[CrossRef](#)] [[PubMed](#)]
13. Yu, L.; Ding, Y.; Zheng, M. Polyoxometalate-based manganese clusters as catalysts for efficient photocatalytic and electrochemical water oxidation. *Appl. Catal. B Environ.* **2017**, *209*, 45–52. [[CrossRef](#)]
14. Geletii, Y.V.; Botar, B.; Kögerler, P.; Hillesheim, D.A.; Musaev, D.G.; Hill, C.L. An All-Inorganic, Stable, and Highly Active Tetra-ruthenium Homogeneous Catalyst for Water Oxidation. *Angew. Chem. Int. Ed.* **2008**, *47*, 3896–3899. [[CrossRef](#)]
15. Du, X.Q.; Zhao, J.L.; Mi, J.Q.; Ding, Y.; Zhou, P.P.; Ma, B.C.; Zhao, J.W.; Song, J. Efficient photocatalytic H₂ evolution catalyzed by an unprecedented robust molecular semiconductor {Fe₁₁} nanocluster without cocatalysts at neutral conditions. *Nano Energy* **2015**, *16*, 247–255. [[CrossRef](#)]
16. Chen, L.; Chen, W.L.; Wang, X.L.; Li, Y.G.; Su, Z.M.; Wang, E.B. Polyoxometalates in dye-sensitized solar cells. *Chem. Soc. Rev.* **2019**, *48*, 260–284. [[CrossRef](#)]
17. Troupis, A.; Hiskia, A.; Papaconstantinou, E. Photocatalytic Reduction and Recovery of Copper by Polyoxometalates. *Environ. Sci. Technol.* **2002**, *36*, 5355–5362. [[CrossRef](#)]

18. Kornarakis, I.; Lykakis, I.N.; Vordos, N.; Armatas, G.S. Efficient visible-light photocatalytic activity by band alignment in mesoporous ternary polyoxometalate–Ag₂S–CdS semiconductors. *Nanoscale* **2014**, *6*, 8694–8703. [[CrossRef](#)]
19. Hu, B.; Wang, P.F.; Hou, J.; Wang, C.; Qian, J.; Zhang, N.N.; Yuan, Q.S. Effects of titanium dioxide (TiO₂) nanoparticles on the photodissolution of particulate organic matter: Insights from fluorescence spectroscopy and environmental implications. *Environ. Pollut.* **2017**, *229*, 19–28. [[CrossRef](#)]
20. Park, H.; Choi, W. Photocatalytic conversion of benzene to phenol using modified TiO₂ and polyoxometalates. *Catal. Today* **2005**, *101*, 291–297. [[CrossRef](#)]
21. Zhao, S.; Zhao, X. Polyoxometalates-derived metal oxides incorporated into graphitic carbon nitride framework for photocatalytic hydrogen peroxide production under visible light. *J. Catal.* **2018**, *366*, 98–106. [[CrossRef](#)]
22. Li, K.X.; Yan, L.S.; Zeng, Z.X.; Luo, S.L.; Luo, X.B.; Liu, X.M.; Guo, H.Q.; Guo, Y.H. Fabrication of H₃PW₁₂O₄₀-doped carbon nitride nanotubes by one-step hydrothermal treatment strategy and their efficient visible-light photocatalytic activity toward representative aqueous persistent organic pollutants degradation. *Appl. Catal. B Environ.* **2014**, *156–157*, 141–152. [[CrossRef](#)]
23. Gamelas, J.A.F.; Evtuguin, D.V.; Esculcas, A.P. Transition metal substituted polyoxometalates supported on amine-functionalized silica. *Transit. Met. Chem.* **2007**, *32*, 1061–1067. [[CrossRef](#)]
24. Sajjad, S.; Leghari, S.A.K.; Iqbal, A. Study of Graphene Oxide Structural Features for Catalytic, Antibacterial, Gas Sensing, and Metals Decontamination Environmental Applications. *ACS Appl. Mater. Inter.* **2017**, *9*, 43393–43414. [[CrossRef](#)] [[PubMed](#)]
25. Kamat, P.V. Graphene-Based Nanoassemblies for Energy Conversion. *J. Phys. Chem. Lett.* **2011**, *2*, 242–251. [[CrossRef](#)]
26. Zhang, N.; Zhang, Y.H.; Xu, Y.J. Recent progress on graphene-based photocatalysts: Current status and future perspectives. *Nanoscale* **2012**, *4*, 5792–5813. [[CrossRef](#)]
27. Liu, J.; Zhang, H.C.; Tang, D.; Zhang, X.; Yan, L.K.; Han, Y.Z.; Huang, H.; Liu, Y.; Kang, Z.H. Carbon Quantum Dot/Silver Nanoparticle/Polyoxometalate Composites as Photocatalysts for Overall Water Splitting in Visible Light. *ChemCatChem* **2014**, *6*, 2634–2641. [[CrossRef](#)]
28. Liu, G.D.; Zhao, X.F.; Zhang, J.; Liu, S.J.; Sha, J.Q. Z-scheme Ag₃PO₄/POM/GO heterojunction with enhanced photocatalytic performance for degradation and water splitting. *Dalton Trans.* **2018**, *47*, 6225–6232. [[CrossRef](#)]
29. Tang, Y.J.; Wang, Y.; Wang, X.L.; Li, S.L.; Huang, W.; Dong, L.Z.; Liu, C.H.; Li, Y.F.; Lan, Y.Q. Molybdenum Disulfide/Nitrogen-Doped Reduced Graphene Oxide Nanocomposite with Enlarged Interlayer Spacing for Electrocatalytic Hydrogen Evolution. *Adv. Energy Mater.* **2016**, *6*, 1600116. [[CrossRef](#)]
30. Tang, Y.J.; Liu, C.H.; Huang, W.; Wang, X.L.; Dong, L.Z.; Li, S.L.; Lan, Y.Q. Bimetallic Carbides-Based Nanocomposite as Superior Electrocatalyst for Oxygen Evolution Reaction. *ACS Appl. Mater. Inter.* **2017**, *9*, 16977–16985. [[CrossRef](#)]
31. Iwase, A.; Ng, Y.H.; Yoshimi, I.; Kudo, A.; Amal, R. Reduced Graphene Oxide as a Solid-State Electron Mediator in Z-Scheme Photocatalytic Water Splitting under Visible Light. *J. Am. Chem. Soc.* **2011**, *133*, 11054–11057. [[CrossRef](#)] [[PubMed](#)]
32. Novoselov, K.S.; Geim, A.K.; Morozov, S.V.; Jiang, D.; Zhang, Y.; Dubonos, S.V.; Grigorieva, I.V.; Firsov, A.A. Electric Field Effect in Atomically Thin Carbon Films. *Science* **2004**, *306*, 666–669. [[CrossRef](#)] [[PubMed](#)]
33. Xiang, Q.J.; Yu, J.G.; Jaroniec, M. Graphene-based semiconductor photocatalysts. *Chem. Soc. Rev.* **2012**, *41*, 782–796. [[CrossRef](#)]
34. Geim, A.K. Graphene: Status and Prospects. *Science* **2009**, *324*, 1530–1534. [[CrossRef](#)] [[PubMed](#)]
35. Wei, T.; Zhang, M.; Wu, P.; Tang, Y.J.; Li, S.L.; Shen, F.C.; Wang, X.L.; Zhou, X.P.; Lan, Y.Q. POM-based metal-organic framework/reduced graphene oxide nanocomposites with hybrid behavior of battery-supercapacitor for superior lithium storage. *Nano Energy* **2017**, *34*, 205–214. [[CrossRef](#)]
36. Li, H.L.; Gupta, J.; Wang, S.; Zhang, N.; Bubeck, C. Photoreduction of graphene oxide with polyoxometalate clusters and its enhanced saturable absorption. *J. Colloid Interface Sci.* **2014**, *427*, 25–28. [[CrossRef](#)] [[PubMed](#)]
37. Huang, Y.Y.; Xiao, A.X.; Hou, G.H.; Li, H.T.; Guo, T.; Guan, B.O. Photocatalysis in an evanescent field: An in situ approach to studying photocatalytic performance by tracing interfacial refractive index changes and kinetics. *J. Mater. Chem. A* **2018**, *6*, 20513–20522. [[CrossRef](#)]
38. Zhang, N.; Yang, M.Q.; Liu, S.Q.; Sun, Y.G.; Xu, Y.J. Waltzing with the Versatile Platform of Graphene to Synthesize Composite Photocatalysts. *Chem. Rev.* **2015**, *115*, 10307–10377. [[CrossRef](#)]

39. Wang, Z.L.; Tan, H.Q.; Chen, W.L.; Li, Y.G.; Wang, E.B. A copper(ii)-ethylenediamine modified polyoxoniobate with photocatalytic H₂ evolution activity under visible light irradiation. *Dalton Trans.* **2012**, *41*, 9882–9884. [[CrossRef](#)]
40. Shen, J.Q.; Zhang, Y.; Zhang, Z.M.; Li, Y.G.; Gao, Y.Q.; Wang, E.B. Polyoxoniobate-based 3D framework materials with photocatalytic hydrogen evolution activity. *Chem. Commun.* **2014**, *50*, 6017–6019. [[CrossRef](#)]
41. Geng, Q.H.; Liu, Q.S.; Ma, P.T.; Wang, J.P.; Niu, J.Y. Synthesis crystal structure and photocatalytic properties of an unprecedented arsenic-disubstituted Lindqvist-type peroxopolyoxoniobate ion: {As₂Nb₄(O₂)₄O₁₄H_{1.5}}^{4.5-}. *Dalton Trans.* **2014**, *43*, 9843–9846. [[CrossRef](#)] [[PubMed](#)]
42. Hu, J.F.; Wang, Y.; Zhang, X.N.; Chi, Y.N.; Yang, S.; Li, J.K.; Hu, C.W. Controllable Assembly of Vanadium-Containing Polyoxoniobate-Based Three-Dimensional Organic-Inorganic Hybrid Compounds and Their Photocatalytic Properties. *Inorg. Chem.* **2016**, *55*, 7501–7507. [[CrossRef](#)] [[PubMed](#)]
43. Niu, J.Y.; Li, F.; Zhao, J.W.; Ma, P.T.; Zhang, D.D.; Bassil, B.; Kortz, U.; Wang, J.P. Tetradecacobalt(II)-Containing 36-Niobate [Co₁₄(OH)₁₆(H₂O)₈Nb₃₆O₁₀₆]²⁰⁻ and Its Photocatalytic H₂ Evolution Activity. *Chem. Eur. J.* **2014**, *20*, 9852–9857. [[CrossRef](#)] [[PubMed](#)]
44. Wu, F.; Xie, A.M.; Sun, M.X.; Wang, Y.; Wang, M.Y. Reduced graphene oxide (RGO) modified spongelike polypyrrole (PPy) aerogel for excellent electromagnetic absorption. *J. Mater. Chem. A* **2015**, *3*, 14358–14369. [[CrossRef](#)]
45. Abaci, U.; Guney, H.Y.; Kadiroglu, U. Morphological and electrochemical properties of PPy, PANi bilayer films and enhanced stability of their electrochromic devices (PPy/PAni–PEDOT, PANi/PPy–PEDOT). *Electrochim. Acta* **2013**, *96*, 214–224. [[CrossRef](#)]
46. Filowitz, M.; Ho, R.K.C.; Klemperer, W.G.; Shum, W. ¹⁷O nuclear magnetic resonance spectroscopy of polyoxometalates. 1. Sensitivity and resolution. *Inorg. Chem.* **1979**, *18*, 93–103. [[CrossRef](#)]
47. Hummers, W.S.; Offeman, R.E. Preparation of Graphitic Oxide. *J. Am. Chem. Soc.* **1958**, *80*, 1339. [[CrossRef](#)]
48. Bao, C.L.; Song, L.; Xing, W.Y.; Yuan, B.H.; Wilkie, C.A.; Huang, J.L.; Guo, Y.Q.; Hu, Y. Preparation of graphene by pressurized oxidation and multiplex reduction and its polymer nanocomposites by masterbatch-based melt blending. *J. Mater. Chem.* **2012**, *22*, 6088–6096. [[CrossRef](#)]
49. Suvina, V.; Krishna, S.M.; Nagaraju, D.H.; Melo, J.S.; Balakrishna, R.G. Polypyrrole-reduced graphene oxide nanocomposite hydrogels: A promising electrode material for the simultaneous detection of multiple heavy metal ions. *Mater. Lett.* **2018**, *232*, 209–212. [[CrossRef](#)]
50. Yin, Y.; Zhang, H.T.; Huang, P.R.; Xiang, C.L.; Zou, Y.J.; Xu, F.; Sun, L.X. Inducement of nanoscale Cu–BTC on nanocomposite of PPy–rGO and its performance in ammonia sensing. *Mater. Res. Bull.* **2018**, *99*, 152–160. [[CrossRef](#)]
51. Liu, R.J.; Li, S.W.; Yu, X.L.; Zhang, G.J.; Zhang, S.J.; Yao, J.N.; Keita, B.; Nadjjo, L.; Zhi, L.J. Facile Synthesis of Au-Nanoparticle/Polyoxometalate/Graphene Tricomponent Nanohybrids: An Enzyme-Free Electrochemical Biosensor for Hydrogen Peroxide. *Small* **2012**, *8*, 1398–1406. [[CrossRef](#)] [[PubMed](#)]
52. Han, Y.Q.; Zhang, Z.L.; Yang, M.; Li, T.X.; Wang, Y.M.; Cao, A.P.; Chen, Z.X. Facile preparation of reduced graphene oxide/polypyrrole nanocomposites with urchin-like microstructure for wide-potential-window supercapacitors. *Electrochim. Acta* **2018**, *289*, 238–247. [[CrossRef](#)]
53. Jiang, Y.Z.; Gu, Y.; Nie, G.D.; Chi, M.Q.; Yang, Z.Z.; Wang, C.; Wei, Y.; Lu, X.F. Synthesis of RGO/Cu₈S₅/PPy Composite Nanosheets with Enhanced Peroxidase-Like Activity for Sensitive Colorimetric Detection of H₂O₂ and Phenol. *Part. Part. Syst. Charact.* **2017**, *3*, 1600233–1600240. [[CrossRef](#)]
54. Gan, Q.Y.; Shi, W.L.; Xing, Y.J.; Hou, Y.A. Polyoxoniobate/g-C₃N₄ Nanoporous Material with High Adsorption Capacity of Methylene Blue from Aqueous Solution. *Front. Chem.* **2018**, *6*, 7–16. [[CrossRef](#)]
55. Aureliano, M.; Ohlin, C.A.; Vieira, M.O.; Marques, M.P.M.; Casey, W.H.; Batista de Carvalho, L.A.E. Characterization of decavanadate and decaniobate solutions by Raman spectroscopy. *Dalton Trans.* **2016**, *45*, 7391–7399. [[CrossRef](#)]
56. Fullmer, L.B.; Malmberg, C.E.; Fast, D.B.; Wills, L.A.; Cheong, P.H.Y.; Dolgos, M.R.; Nyman, M. Aqueous tantalum polyoxometalate reactivity with peroxide. *Dalton Trans.* **2017**, *46*, 8486–8493. [[CrossRef](#)]
57. Akhavan, O.; Ghaderi, E. Photocatalytic Reduction of Graphene Oxide Nanosheets on TiO₂ Thin Film for Photoinactivation of Bacteria in Solar Light Irradiation. *J. Phys. Chem. C* **2009**, *113*, 20214–20220. [[CrossRef](#)]
58. Ma, J.; He, Y.; Shi, H.; Fan, Y.; Yu, H.; Li, Y.B. Stable graphene oxide-based composite membranes intercalated with montmorillonite nanoplatelets for water purification. *J. Mater. Sci.* **2019**, *54*, 2241–2255. [[CrossRef](#)]

59. Zhang, L.B.; Li, X.T.; Wang, X.H.; Han, L.; Liu, R.Y.; Zheng, B.B.; Li, W.T.; Liu, X.L.; Liu, Y.C. Photo-assisted preparation and patterning of large-area reduced graphene oxide-TiO₂ conductive thin film. *Chem. Commun.* **2010**, *46*, 3499–3501.
60. Liu, Q.Q.; Shen, J.Y.; Yang, X.F.; Zhang, T.R.; Tang, H. 3D reduced graphene oxide aerogel-mediated Z-scheme photocatalytic system for highly efficient solar-driven water oxidation and removal of antibiotics. *Appl. Catal. B Environ.* **2018**, *232*, 562–573. [[CrossRef](#)]
61. Bai, X.; Du, Y.Y.; Hu, X.Y.; He, Y.D.; He, C.L.; Liu, E.Z.; Fan, J. Synergy removal of Cr (VI) and organic pollutants over RP-MoS₂/rGO photocatalyst. *Appl. Catal. B Environ.* **2018**, *239*, 204–213. [[CrossRef](#)]
62. Yang, J.; Huang, J.H.; Fan, D.Y.; Chen, S.H. First-principles investigation on the electronic property and bonding configuration of NbC (111)/NbN (111) interface. *J. Alloys Compd.* **2016**, *689*, 874–884. [[CrossRef](#)]
63. Kulkarni, A.K.; Praveen, C.S.; Sethi, Y.A.; Panman, R.P.; Arbu, S.S.; Naik, S.D.; Ghule, A.V.; Kale, B.B. Nanostructured N-doped orthorhombic Nb₂O₅ as an efficient stable photocatalyst for hydrogen generation under visible light. *Dalton Trans.* **2017**, *46*, 14859–14868. [[CrossRef](#)] [[PubMed](#)]
64. Ma, L.F.; Li, F.Y.; Sun, Z.X.; Liu, M.M.; Wang, Y.H.; Xu, L. Synergetic effect of polyoxoniobate and NiS as cocatalysts for enhanced photocatalytic H₂ evolution on Cd_{0.65}Zn_{0.35}S. *RSC Adv.* **2014**, *4*, 21369–21372. [[CrossRef](#)]
65. Li, T.; Wang, K.; Fang, Q.T.; Zhang, Y.; Wang, B.; Li, R.; Lin, Y.Z.; Liu, K.C.; Xie, H.Q.; Li, K. Conductive polymer supported and confined iron phosphide nanocrystals for boosting the photocatalytic hydrogen production of graphitic carbon nitride. *J. Mater. Chem. C* **2020**, *8*, 14540–14547. [[CrossRef](#)]
66. Zhang, W.Y.; Shen, C.; Lu, G.X.; Ni, Y.R.; Lu, C.H.; Xu, Z.Z. Synthesis of PPy/RGO-based hierarchical material with super-paramagnetic behavior and understanding its robust photo current driven by visible light. *Synth. Met.* **2018**, *241*, 17–25. [[CrossRef](#)]
67. Yuan, X.J.; Drago, D.; Beaunier, P.; Uribe, D.B.; Ramos, L.; Méndez-Medrano, M.G.; Remita, H. Polypyrrole nanostructures modified with mono and bimetallic nanoparticles for photocatalytic H₂ generation. *J. Mater. Chem. A* **2020**, *8*, 268–277. [[CrossRef](#)]
68. Wang, K.L.; Endo-Kimura, M.; Belchi, R.; Zhang, D.; Habert, A.; Bouclé, J.; Ohtani, B.; Kowalska, E.; Herlin-Boime, N. Carbon/Graphene-Modified Titania with Enhanced Photocatalytic Activity under UV and Vis Irradiation. *Materials* **2019**, *12*, 4158. [[CrossRef](#)]
69. Yuan, X.J.; Floresyona, D.; Aubert, P.H.; Bui, T.T.; Remita, S.; Ghosh, S.; Brisset, F.; Fabrice, G.; Remita, H. Photocatalytic degradation of organic pollutant with polypyrrole nanostructures under UV and visible light. *Appl. Catal. B Environ.* **2019**, *242*, 284–292. [[CrossRef](#)]

Publisher's Note: MDPI stays neutral with regard to jurisdictional claims in published maps and institutional affiliations.



© 2020 by the authors. Licensee MDPI, Basel, Switzerland. This article is an open access article distributed under the terms and conditions of the Creative Commons Attribution (CC BY) license (<http://creativecommons.org/licenses/by/4.0/>).